Appl. Phys. B 79, 775–782 (2004)
DOI: 10.1007/s00340-004-1631-2

Applied Physics B
Lasers and Optics

I. BALIN[1]
I. SERIKOV[3]
S. BOBROVNIKOV[3]
V. SIMEONOV[1,✉]
B. CALPINI[1,2]
Y. ARSHINOV[3]
H. VAN DEN BERGH[1]

Simultaneous measurement of atmospheric temperature, humidity, and aerosol extinction and backscatter coefficients by a combined vibrational–pure-rotational Raman lidar

[1] Air and Soil Pollution Laboratory (LPAS), Swiss Federal Institute of Technology (EPFL), 1015 Lausanne, Switzerland
[2] Aerological Station, MeteoSwiss, 1530 Payerne, Switzerland
[3] Institute of Atmospheric Optics (IAO), SB RAS, Tomsk, Russia

Received: 13 May 2004
Published online: 8 September 2004 •

ABSTRACT Implementation of the pure-rotational Raman (PRR) lidar method for simultaneous measurement of atmospheric temperature, humidity, and aerosol extinction and backscatter coefficients is reported. The isolation of two wavelength domains of the PRR spectrum and the suppression of the elastically scattered light is carried out by a double-grating polychromator. Experiments involving elastic backscatter from dense clouds and a solid target confirm the high level of suppression of the elastic light in the corresponding acquisition channels of the two selected PRR domains. Calibration of the temperature channel was done both by comparison with an experimentally verified atmospheric temperature model profile and by inter-comparison with radiosondes. Night-time temperature profiles with high vertical resolution were obtained up to the lower stratosphere. The PRR temperature profile combined with the water vapor mixing ratio obtained from the ro-vibrational Raman channel is used to estimate the relative humidity.

PACS 42.68.Wt; 42.68.Mj; 33.20.Fb

1 Introduction

Simultaneous measurements of vertical profiles of atmospheric temperature, water vapor, and aerosol optical properties (i.e. backscatter and extinction coefficients) are required for the retrieval and interpretation of the relative humidity (RH) of the atmosphere, as well as the height and the dynamics of the planetary boundary layer (PBL). Vertical temperature and humidity profiles are usually obtained worldwide by systematic radiosonde measurements. The temporal resolution of these observations is quite low, typically two radiosonde launches a day, with a single data readout per height bin. As a result, the measured profiles are often not representative of some important weather phenomena, such as the development of a convective boundary layer or the passage of a cold front, which cannot be resolved due to the lack of time resolution. Furthermore, the standard radiosondes are not equipped with instruments for aerosol measurements.

Alternative remote-sensing techniques like lidar can be very useful for supplying temperature, humidity, and aerosol data with high temporal and spatial resolution. The two lidar techniques used for temperature profiling are the Rayleigh and the pure-rotational Raman methods. The Rayleigh approach [1] exploits the proportionality of the molecular lidar signal to the atmospheric density. It requires density and pressure data at a relatively high altitude (30–40 km) as a starting point for the retrieval and assumes the existence of hydrostatic equilibrium throughout the entire atmospheric column below this point. In addition, the method is not applicable for atmospheric layers with a significant aerosol load [2] and can be mainly used in stratospheric regions which are essentially free of aerosols [3]. The Rayleigh method can also be used for lower altitudes if a vibrational Raman signal from atmospheric nitrogen is employed to compensate for the aerosol influence [4].

Cooney [5] was the first to propose the use of the temperature dependence of the pure-rotational Raman (PRR) spectra of atmospheric N_2 and O_2 molecules for temperature profiling. The temperature is deduced from the intensity ratio of two PRR signals corresponding to the two selected domains from Stokes and anti-Stokes spectral bands of N_2 and O_2 [6, 7], which have reverse temperature dependence. Because of the low cross section of the spontaneous Raman scattering, the PRR lidar signals are six orders of magnitude weaker than the elastic signal. To prevent the contamination of the Raman signals with spurious light from the elastic scattering, spectral selection devices with higher than 10^8 out-of-band rejection rates have to be used. For that reason the PRR signals are usually isolated by narrow-band interference filters or diffraction-grating-based instruments. The interference filters are easy to use and have a relatively high transmission and out-of-band rejection of up to 10^6. However, their bandwidth and their central wavelength position are sensitive to temperature variations and are affected by aging and long-term drifts [8]. Grating-based instruments have lower rejection (typically 10^4–10^5) and to achieve the necessary rejection rates they have to be used either in combination with atomic resonance absorption filters or as double-grating devices [9]. The advantages of the grating-based instruments are their proven long-term stability and the possibility to sum optically the signals from the Stokes and anti-Stokes branches having the same temperature dependence, which thus will enhance the signal to noise ratio [9]. Further improvement in the technique for daytime operation aimed at signal-to-

✉ Fax: +41-21-693-5145, E-mail: valentin.simeonov@epfl.ch

background enhancement can be achieved by employing an additional Fabry–Perot interferometer (FPI) with a free spectral range equal to the spectral spacing between the nitrogen PRR lines [10]. The FPI cuts out the unwanted daylight background from the spectral gaps between the PRR lines while transmitting efficiently the rotational lines at the same time.

Aerosol extinction profiles are usually measured by elastic backscatter lidars. To retrieve the extinction coefficient by inverting the elastic-lidar equation, in the most frequently used Fernald or Klett approaches, the aerosol extinction-to-backscatter ratio and the extinction at a reference altitude have to be assumed [11, 12]. By using a vibrational Raman signal from nitrogen, the retrieval of the aerosol extinction coefficient becomes possible [13] with the only assumption being about the wavelength dependence of the aerosol extinction [14], which is supposed to remain constant over the wavelength interval of interest.

The aerosol extinction can be obtained from the PRR signal without any assumption about aerosol and atmospheric optical properties because of the spectral closeness of the PRR lines and the elastically backscattered (i.e. Cabannes) line. The main obstacle for aerosol measurements, i.e. the temperature dependence of the PRR signal, can be solved by using the sum of the lidar returns from the Stokes and anti-Stokes PRR branches, which sum is practically temperature independent.

In this paper, we present the addition of a pure-rotational Raman channel to an existing multi-wavelength elastic-ro-vibrational-Raman lidar in order to obtain temperature, aerosol extinction, and backscatter measurements [15] as well as information on the height-resolved relative humidity. The algorithms for the retrieval of the temperature, the backscatter, the extinction, and the lidar ratio based on the rotational Raman-lidar technique and the water vapor mixing ratio based on vibrational Raman signals [16] are summarized below. Finally, we will describe the instrument and its performance, illustrated by a set of measurements, which are compared with techniques accepted as standard methods.

2 Method

2.1 *Algorithms for atmospheric retrievals*

2.1.1 Temperature. The lidar method exploits the reverse temperature dependence of the low- and high-quantum-number transition intensities of the air PRR spectra (PRRS). To enhance the signal level, the parts symmetric to the Cabannes line (same temperature dependence) from the S and O branches are optically summed as explained below in the system description (Sect. 2.2). The temperature T at elevation Z is derived from the ratio of the intensity of the lidar signals corresponding to the parts of the PRRS with low $S_{\mathrm{JL}}(Z)$ and high $S_{\mathrm{JH}}(Z)$ [5, 9] rotational quantum numbers using the following approximate relationship:

$$T(Z) = \frac{A}{\ln \frac{S_{\mathrm{JL}}(Z)}{S_{\mathrm{JH}}(Z)} + B} \,. \tag{1}$$

The accuracy of (1) is $\pm 1^\circ$ within the temperature range of 220–310 K. The constants A and B are determined by lidar calibration.

The statistical error (δT_{stat}) is calculated from the lidar signals, assuming their statistical independence and the validity of the Poisson statistics as

$$\delta T_{\mathrm{stat}}(Z) = \frac{A}{\left[\ln \frac{S_{\mathrm{JL}}(Z)}{S_{\mathrm{JH}}(Z)} + B\right]^2} \sqrt{\left(\frac{\delta S_{\mathrm{JL}}(Z)}{S_{\mathrm{JL}}(Z)}\right)^2 + \left(\frac{\delta S_{\mathrm{JH}}(Z)}{S_{\mathrm{JH}}(Z)}\right)^2} \,. \tag{2}$$

The calibration errors (δT_{AB}) due to inaccuracy of the calibration constants A and B are calculated following the standard error-propagation technique.

2.1.2 Aerosol backscatter and extinction. To measure the aerosol extinction by the PRR method we use the sum S_{R}:

$$\begin{aligned} S_{\mathrm{R}}(Z) &= S_{\mathrm{JL}}(Z) + S_{\mathrm{JH}}(Z) \\ &= \mathrm{const} \frac{1}{Z^2} \beta_{\mathrm{R}}(Z) \exp\left[-2 \int_{Z_0}^{Z} [\alpha_{\mathrm{m}}(z) + \alpha_{\mathrm{a}}(z)] \,\mathrm{d}z\right] , \end{aligned} \tag{3}$$

where β_{R} is the Raman backscattering and α_{a} and α_{m} are correspondingly the aerosol and molecular extinction coefficients. It can easily be shown by direct calculation that S_{R} is practically temperature independent for suitably selected $S_{\mathrm{JL}}(Z)$ and $S_{\mathrm{JH}}(Z)$. The aerosol extinction is then derived as

$$\alpha_{\mathrm{a}}(Z) = -\frac{1}{2} \frac{\mathrm{d}}{\mathrm{d}z} \left[\ln \frac{S_R(Z)}{S_m(Z)}\right] , \tag{4}$$

where $S_{\mathrm{m}}(Z)$ is a simulated molecular lidar signal. In this work, we calculated $S_{\mathrm{m}}(z)$ following [17] and using air number density profiles based on the US Standard Atmosphere model [18] initialized with the temperature and pressure values measured at the lidar site. In (4) the extinction-wavelength dependences are neglected because of the small separation between the excitation and scattered wavelengths.

The total extinction $\alpha(Z)$ is then obtained as a sum of the particle $\alpha_{\mathrm{a}}(Z)$ and the calculated molecular extinction $\alpha_{\mathrm{m}}(Z)$ profiles. Finally, the total backscatter coefficient $\beta(z)$ is retrieved from the extinction profile and the elastic signal measured at the excitation wavelength $S_{\mathrm{E}}(z)$:

$$\beta(Z) = \frac{Z^2}{K_{\mathrm{s}}} S_{\mathrm{E}}(Z) \exp\left[2 \int_{Z_0}^{Z} \alpha(z) \,\mathrm{d}z\right] . \tag{5}$$

The system constant K_{s} is found by normalizing the backscatter profile to a pure molecular signal at a reference altitude defined with the help of the sum signal S_{R}.

The scattering (total to molecular backscatter) ratio is retrieved from the $S_{\mathrm{E}}/S_{\mathrm{R}}$ ratio for altitudes with complete overlap. The proportionality constant between the scattering ratio and the $S_{\mathrm{E}}/S_{\mathrm{R}}$ ratio is derived from measurements taken in aerosol-free conditions.

2.1.3 Water vapor mixing ratio. The water vapor mixing ratio profile $q_{\mathrm{H_2O}}(Z)$ is retrieved [19] from the water vapor (407-nm) and nitrogen (387-nm) vibrational Raman signals excited

with 355-nm radiation:

$$q_{H_2O}(Z) = K_{H_2O}(Z)\frac{S_{H_2O}(Z)_{407} - b_{407}(Z)}{S_{N_2}(Z)_{387} - b_{387}(Z)} \times \exp\left[\int_{Z_0}^{Z} \alpha_{407}(z) - \alpha_{387}(z)\,dz\right], \quad (6)$$

where S and b denote correspondingly the Raman signals and the background noise in the respective channels. The calibration is based on the in situ water vapor mixing ratio value, calculated from the meteorological data (RH, T, and P) gathered at the lidar site. The term under the exponent is the differential atmospheric extinction on the return path at the nitrogen and water Raman-shifted wavelengths. It can be divided into molecular and aerosol differential extinctions. The molecular differential extinction is calculated from the atmospheric models and does not exceed 4% in the tropopause. The aerosol differential absorption can often be neglected in the upper tropospheric and the lower stratospheric regions because of the low aerosol load (aerosol optical density (AOD) < 0.05 [20]) but has to be taken into account for AOD > 0.3 [21], as is the case for events of Saharan dust transport, PBL intrusions, volcanic ash, or in the presence of thin clouds. When AOD > 0.3, the differential aerosol extinction is calculated from the extinction coefficient (α_a) at 387 nm derived from (4) and then extrapolated with the Angström power law to 407 nm. The differential absorption by gases can be neglected [19] at these wavelengths in the upper troposphere. These corrections are more significant at the UV wavelengths for water-vapor measurements in the planetary boundary layer [22]. The atmospheric relative humidity is then calculated from the water vapor mixing ratio and the temperature profiles as in [21].

2.2 *Lidar setup*

The lidar is based on a system developed at the Swiss Federal Institute of Technology in Lausanne to measure atmospheric extinction and backscatter at three wavelengths together with the water vapor mixing ratio. This lidar has been in operation on a regular basis within the European Aerosol Lidar Network EARLINET [24] since May 2000 at the high-alpine research station Jungfraujoch (3580 m, 46.55° N, 7.98° E) in the Swiss Alps. Water vapor mixing ratio profiles have been systematically measured since August 2000 [23]. A detailed description of the lidar is given in [15]. Here we present only the salient features of the original system, focusing mostly on modifications.

A simplified optical layout of the upgraded system is shown in Fig. 1. The lidar transmitter uses a tripled Nd:YAG laser, producing 3.5-ns pulses with energies of up to 400 mJ at 1064 nm, at a repetition rate that can be tuned continuously from 2 to 100 Hz. The data used in this work was obtained with the laser operated with 300 mJ/pulse at 1064 nm and a repetition rate of 50 Hz. Two thermally controlled BBO crystals perform doubling and tripling of the infrared radia-

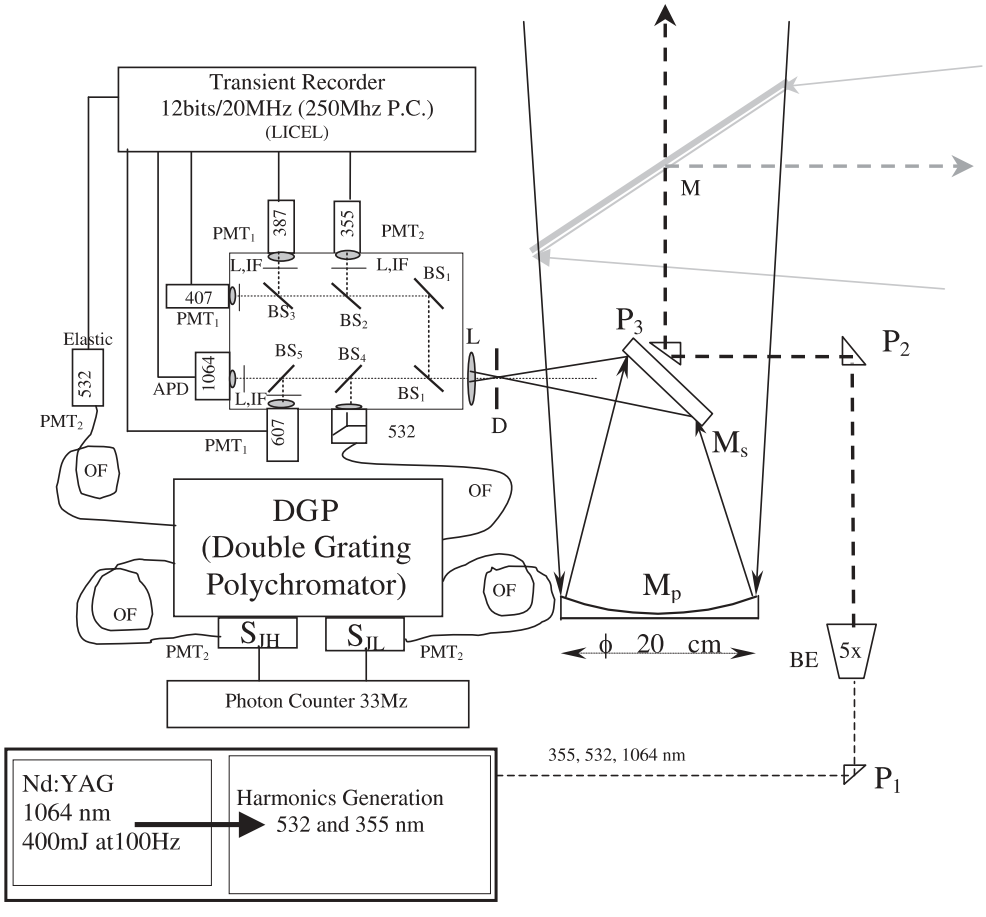

FIGURE 1 Optical layout of the lidar. DGP, double-grating polychromator; L, lens; IF, interference filter; D, diaphragm; M, removable steering mirror; PMT_1, Thorn EMI QA9829; PMT_2, Hamamatsu photosensor modules (H6780-06 and H7421-40); APD, avalanche photodiode; BS, dichroic beam splitter; OF, optical fiber; BE, beam expander; P_i, guidance and alignment prisms

tion. A single, three-wavelength beam expander is employed. This unique beam expander makes possible the use of a coaxial configuration, and hence horizontal and slant-path measurements by employing a steering mirror. Furthermore, because of the simplified design, the transmitter configuration is less affected by mechanical and thermal perturbations, which contributes to the long-term stability of the lidar. The beam expander is a refractive type, with a magnification of $\times 5$, providing a final beam divergence better than 0.14 mrad for all three wavelengths.

The lidar receiver is based on a 20-cm diameter, f/4 Newtonian telescope. The receiver field of view (FOV) can be adjusted from 0.5 to 3.5 mrad by exchangeable diaphragms. A removable 45° steering mirror is used for horizontal measurements. This mirror is aluminum coated, $210 \times 300 \times 40$ mm, and flat to $\lambda/10$ p-v at 633 nm.

The initial spectral separation of the optical signals is carried out by a modified version of the filter–polychromator described in [15]. The polychromator isolates elastic 355-, 532-, and 1064-nm signals as well as N_2 vibrational Raman signals at 387 and 608 nm, and the H_2O Raman signal at 407 nm, by means of dichroic mirrors and interference filters. The polychromator modification concerns only the 532-nm channel which is used for temperature and aerosol measurements associated with the PRR method. In this channel, the existing depolarization unit was replaced by a double-grating polychromator (DGP) that selects four portions from the Stokes and anti-Stokes branches of the PRRS centered on the excitation 532-nm wavelength. The double-polychromator configuration is necessary to achieve a suppression level for the elastically scattered light higher than 10^8. The input of the DGP is connected to the 532-nm output of the filter–polychromator via a 600-μm-core diameter multi-mode silica fiber. The fiber also serves as a scrambler and as an entrance slit for the first part of the DGP, and the fiber diameter defines the overlap function of the lidar temperature channel.

The DGP consists of two identical, Littrow-configuration polychromators, based on 600-gr/mm gratings blazed at 53° and operated in the fifth order. Achromatic doublet lenses perform the collimation and the imaging in the polychromators. The inverse linear dispersion of each of the two parts is ~ 1.0 nm/mm. Four fused-silica fibers with core diameters of 600 μm connect the two parts of the DGP operated in a dispersion-subtraction mode. As a result, the radiation of the pairs symmetric to the 532-nm line is optically summed at the exit of the second polychromator, leading to the signal enhancement. The output optical fibers have a core diameter of 1300 μm and deliver the signal to the detecting photomultiplier tubes (PMTs). The elastic signal at 532 nm is taken from the first part of the DGP by a 600-μm fiber. Details of the DGP design can be found in [25].

The 355-nm and 532-nm elastic signals are detected by Hamamatsu (H6780-06) photosensor modules. Thorn EMI (QA9829) PMTs are used for the detection of 387-, 408-, and 607-nm vibrational Raman signals. Hamamatsu photon-counting modules, model H7421-40, detect the pure-rotational Raman signals. The original TTL forming stage in the electronic block of the modules was eliminated because it caused a reduction in the counting rate. A Si avalanche photodiode (EG&G) detects the 1064-nm radiation.

All detected signals, with the exception of pure-rotational Raman signals, are acquired by seven 12-bit/20 MHz ADC, 250 MHz counting rate transient recorders (Licel), operated in analog and photon-counting modes. A separate multichannel scaler MS 8/10 developed at IOA acquires the PRR signals. The transient digitizers are controlled by a PC via LabView-based software. A second computer controls the multi-channel scaler under Delphy 6-based custom software.

3 Results and discussion

The first step towards regular operation of the temperature channel was to determine the calibration constants A and B in (1). They were initially obtained by non-linear fitting of the lidar and the model temperature profiles. The model profile was calculated according to the US Standard Atmosphere [18] initialized with pressure and temperature values measured in situ at the lidar altitude (3580 m). To verify the applicability of the atmospheric model, a simulated pure molecular (Rayleigh) lidar profile S_m, calculated from the model-derived density, was compared to a S_R profile. The lidar profile was taken on the night of 27th July 2002 in the middle of a four-day period of high pressure and negligible aerosol-load conditions. The simulated and the lidar profiles were fitted at an altitude of 7500 m. The result of this comparison is presented in Fig. 2a. The almost perfect agreement between the two profiles shows, firstly, that the atmospheric model describes adequately the air density, i.e. the temperature and pressure profiles above the Jungfraujoch and, secondly, that the sum PRR signal S_R depends on the temperature only through the air density as given by the ideal gas law. The calibration-constant values retrieved by using the model temperature are correspondingly $A = 310.8$ K and $B = 0.67$. We derived the A and B values for the same lidar measurements by fitting a lidar to a radiosonde temperature profile, assuming horizontal homogeneity of the atmosphere. Since the measurements were taken in the middle of a period of stable, high atmospheric pressure conditions, such an assumption seems to be reasonable. The radiosonde was launched during the lidar measurement from Payerne, situated approximately 80 km west of the Jungfraujoch. The A and B values derived from the radiosonde comparison are correspondingly 307.1 K and 0.66. The model, the radiosonde, and the lidar temperature profiles for 27th July are presented in Fig. 2b. All three profiles clearly show the tropopause height at $\sim 14\,000$ m. The lidar and the radiosonde data are in good agreement for the lower part of the profile, as seen from the scattered plot presented in Fig. 2c. The most serious discrepancies are observed in the tropopause region where both instruments and especially the lidar have lower accuracy. The statistical error (1σ) of the lidar is lower than 0.5 K for altitudes below 9500 m. It is estimated to be 1.5 K at the top of the troposphere and it reaches values of 4.5 K at the highest point of the profile. To estimate the reliability of the calibration method, we also studied the variance of the calibration constants, derived from a comparison between the lidar and the radiosonde temperature profiles. The average values of A and B derived by fitting the lidar profiles to eight radiosonde profiles, taken in July 2002 (four profiles) and August 2003 (four profiles), are correspondingly $A = 301.8$ (min. 298.4, max. 307.1) and

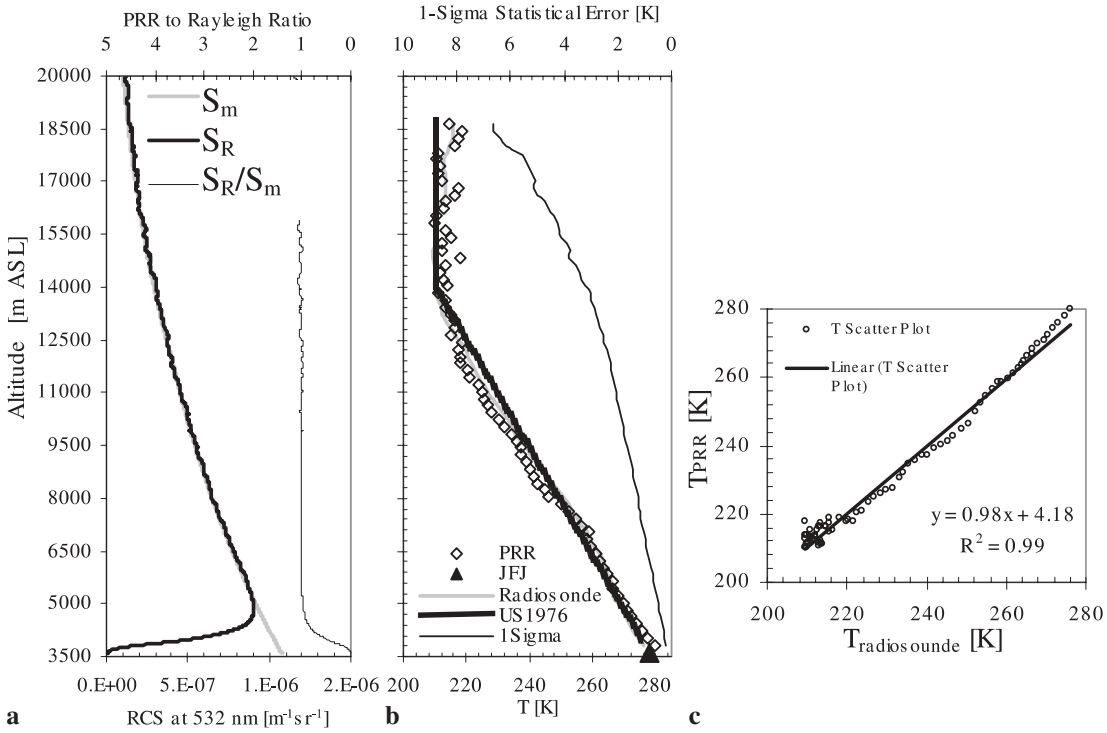

FIGURE 2 **a** Range-corrected sum PRR signal (S_R), simulated Rayleigh signal (S_m), and their ratio; **b** PRR, Payerne radiosonde, and US-1976 model temperature profiles together with the lidar statistical error estimation, JFJ – the temperature at the Jungfraujoch station; **c** scatter plot between radiosonde and PRR temperature profiles. The radiosonde was launched from Payerne at 01:00 h LT. The gliding average, for the retrieval of the temperature profile, used a window of 1000 m with a 200-m step for ~ 30-min integration time

$B = 0.65$ (min. 0.62, max. 0.67). The calibration-constant values show a relatively low variance and their values do not differ by more than 4% for A and 8% for B from the values determined by the atmospheric model calibration method. The differences appear to be mostly due to the retrieval of A and B, which is based on the comparison of data obtained by different radiosondes and by using different time and space averaging of the lidar data profiles. Furthermore, the radiosondes and the lidar, with rare exceptions, sample different air masses even if the balloon is launched from the lidar site. Differences of 1% for A and B lead to temperature errors of correspondingly ~ 1% and 0.5%. Therefore, to achieve a better calibration, more accurate measurements are needed. Since the A and B values depend mostly on the relative position of the PRR spectrum portions used for temperature retrieval, i.e. on the parameters of the DGP, an absolute calibration of the lidar is possible. Such a calibration can be performed by observing the Raman scattering from the air at different temperatures in laboratory conditions using only the DGP and the photodetectors of the lidar receiver.

We performed some tests in order to verify the rejection level at the excitation wavelength in the PRR channels. The initial test measurements were taken in weather conditions with optically dense clouds producing intense backscatter. The simultaneously measured range-corrected 532-nm elastic and PRR sum signals, presented in Fig. 3a, clearly demonstrate that there is no enhancement in the PRR sum signal within the cloud, i.e. there is no cross-talk even for total-to-molecular backscatter ratio values exceeding 70. This ratio, shown in the same figure, was obtained by normalizing the elastic to sum PRR signals ratio to the pure molecular scattering in the aerosol-free region around 5000 m. The PRR night-time profiles of the aerosol extinction and backscatter at 532 nm are presented in Fig. 3b. They show maximum extinction of up to 8×10^{-4} m^{-1} and strong backscatter of up to 0.4×10^{-4} m^{-1} sr^{-1} in the cloud at an altitude of 11 000 m. The temperature profile retrieved from the same measurement and shown in Fig. 3c follows the radiosonde profile but reveals local features. For example, two temperature inversions, one below, and the other near the cloud base, are well pronounced. The second inversion is linked to the cloud stratification and corresponds to the cloud region with lower backscatter and extinction, i.e. lower cloud particle concentration.

In the subsequent tests, we used scattering from a topographic target. The lidar was pointed at a steep, snow-covered mountain slope at ~ 8-km distance. The PRR sum signal (S_R) shows no increase at 8 km, whereas the corresponding 532-nm elastic signal at the same distance saturates and even shows some degree of overshoot (see Fig. 4b). During the test period, preliminary measurements of the aerosol extinction, water vapor, and temperature along a horizontal optical path above the Aletsch glacier have been carried out. The data will be used for a comparative study of the aerosol optical properties derived from the lidar and from in situ measurements [26]. The measurements presented here were taken at night, in stable weather conditions with the lidar pointing in the southern direction. A map of the region with the lidar optical path marked by a dashed line is shown in Fig. 4a. Temperature and water vapor mixing ratio profiles are presented in Fig. 4c, together with a cross section of the terrain below the lidar optical path. The extinction of the order of 10^{-4} m^{-1} and the water vapor mixing ratio values between

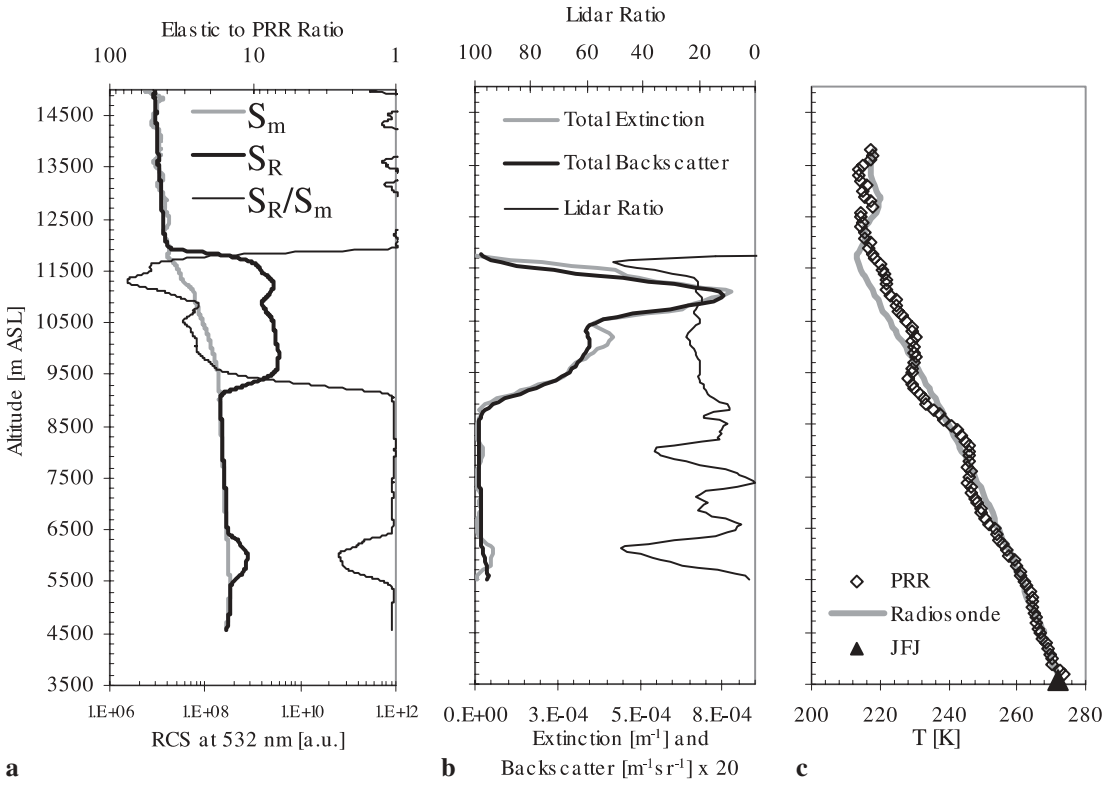

FIGURE 3 **a** Range-corrected sum PRR (S_R) and elastic (S_E) signals, and the S_E/S_R ratio; **b** lidar ratio, backscatter and extinction coefficients; **c** lidar and radiosonde temperature profiles. The profiles were taken on 13.05.2001 between 23:00 and 23:30 h LT

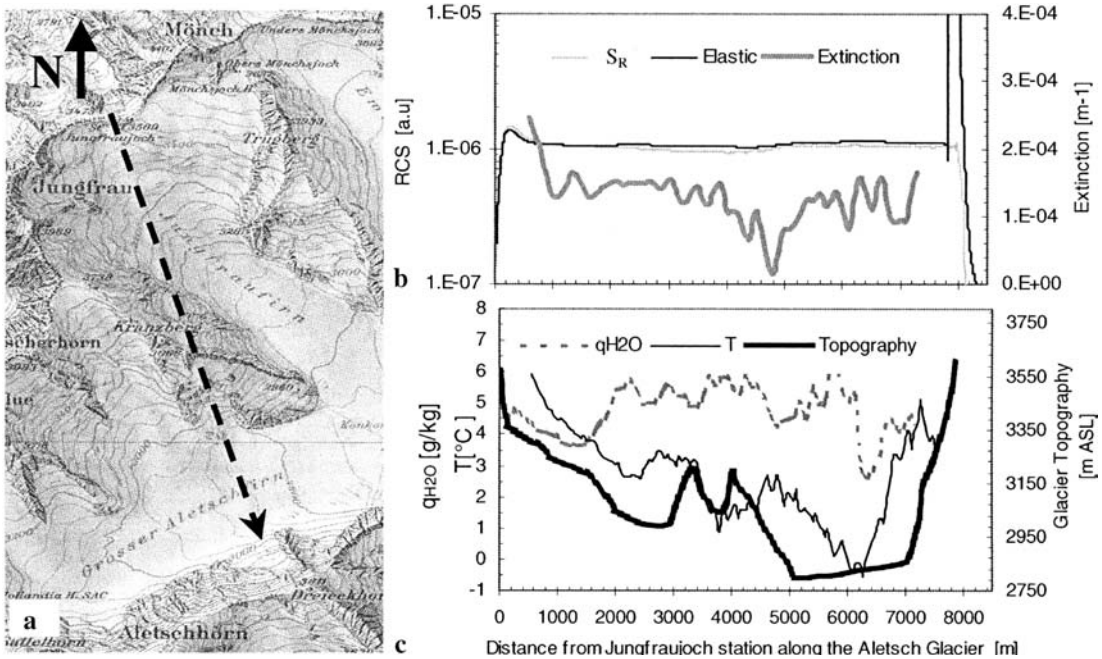

FIGURE 4 **a** Laser-beam trajectory during the horizontal observations above the Aletsch glacier, **b** range-corrected sum PRR and elastic signals together with the total extinction coefficient derived from the PRR signal, **c** topography of the glacier below the laser-beam path from a 1 : 100 000 map (Swiss Topographic Institute), horizontal water vapor mixing ratio, and temperature lidar profiles. The measurements were taken on 27.07.2002 between 2:00 and 4:30 h LT

2.5 and 6.5 g/kg are relatively high and indicate hazy conditions. The temperature varies from 5 °C at the station to almost 0 °C above the deepest valley. Both the water vapor mixing ratio and the temperature suggest an influence of the glacier topography. It should be noted that the temperature and the water vapor content decreased above the valley and increased near to the mountain surface. This example demonstrates the potential of the method to measure simultaneously atmospheric extinction, temperature, and water vapor over the glacier. More systematic observations may

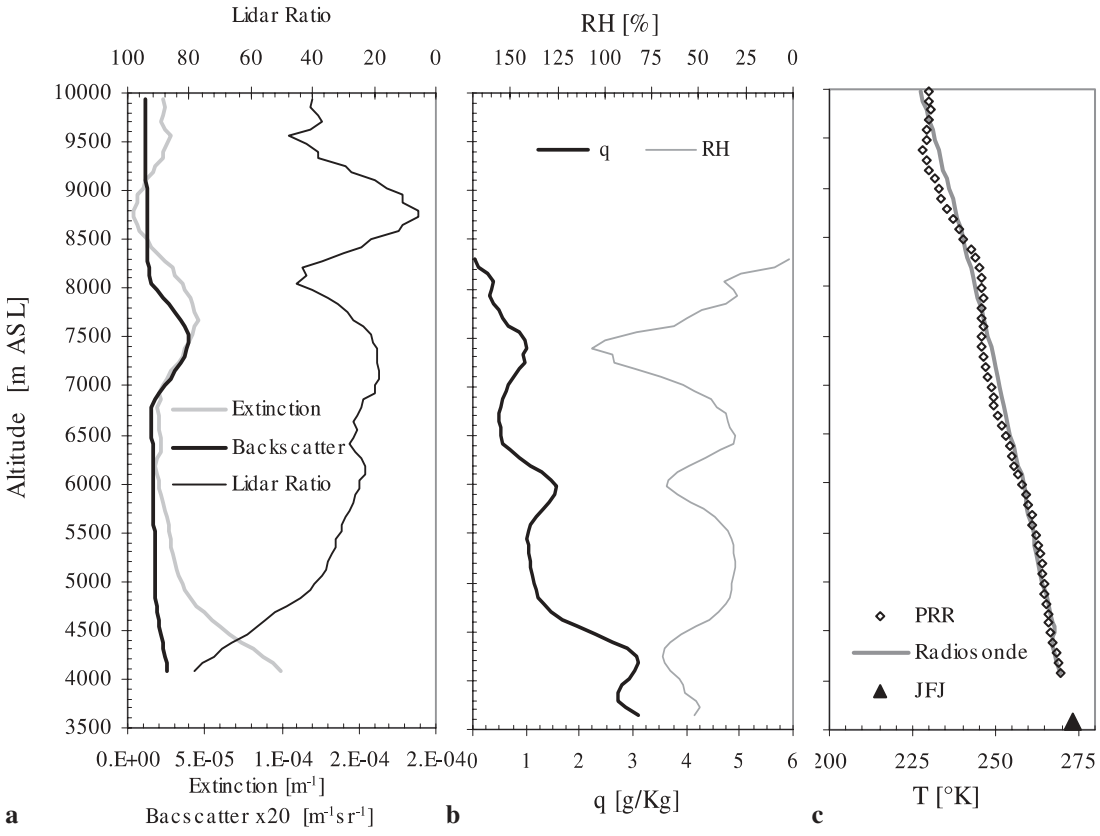

FIGURE 5 **a** Extinction, backscatter, and lidar ratio derived by the PRR method, **b** water vapor mixing ratio and relative humidity, **c** lidar and radiosonde temperature profiles. The measurements were taken on 24.07.2002 between 1:00 and 2:00 h LT

provide useful data for the estimation of the atmospheric dynamics over complex terrains, particularly over those covered by glaciers [27].

Simultaneous measurements of extinction, backscatter, lidar ratio, water vapor mixing ratio, relative humidity, and temperature have been taken at regular intervals with the lidar since June 2002. The vertical profiles measured on 24th July 2002 are presented in Fig. 5 as an example. In the water vapor and aerosol profiles several atmospheric layers can be identified, some of which are noticeable also in the temperature profile. The cirrus cloud between 7 and 8 km is well defined, with relative humidity exceeding 100% and a lidar ratio of up to 45. The temperature profile follows the general wet lapse rate of ~ 6.7 K/km recorded by the radiosonde and reveals some local features such as the temperature inversion in the upper part of the cirrus cloud. The lower part of the atmosphere (up to ~ 4700 m) is characterized by high specific humidity of up to 3 g/kg (RH above 70%). The high humidity is probably the reason for the high extinction observed up to this altitude. Despite the high relative humidity of above 70% measured at 6000 m, there is no formation of any aerosol layer, as can be seen from the extinction and backscatter profiles, while at ~ 7500 m, in super-saturation conditions, a cloud forms.

4 Conclusion

We report the implementation on the existing Jungfraujoch multi-wavelength elastic-Raman lidar of the PRR method for measurement of temperature, aerosol extinction and backscatter coefficients, and the relative humidity. The portions of the PRR signals are isolated by a double-grating polychromator. This technique shows better immunity against contamination of the PRR signals with elastically scattered light compared to interference filter based polychromators. The high level of suppression of the elastic light in the PRR channels is demonstrated by measurements in a dense cloud with scattering ratio higher than 70 and by scattering from a solid target. A method based on comparison with an experimentally verified atmospheric model was used for calibration of the temperature channel. Inter-comparison calibration measurements with a radiosonde show good agreement.

The use of the PRR technique for direct calculation of the total to molecular backscatter ratio, the backscatter, the extinction coefficients, and the lidar ratio, is presented. Nighttime temperature profiles, measured by the PRR technique, were obtained up to the lower stratosphere, with a 30-min time average and a high vertical resolution $\sim$ 200–500 m. The PRR temperature profile was used in combination with the water vapor mixing ratio for estimation of the relative humidity.

ACKNOWLEDGEMENTS We acknowledge the Swiss National Science Foundation for financial support under Grant No. 2000-66932.01 and we are grateful to MeteoSwiss for their collaboration and for supplying us with valuable meteorological data. Special thanks are given to the International Foundation High Altitude Research Stations Jungfraujoch and Gornergrat for providing the logistics support.

REFERENCES

1 A. Hauchecorne, M.L. Chanin: Geophys. Res. Lett. **7**, 565 (1980)
2 M.R. Gross, T.J. McGee, R.A. Ferrare, U.N. Singh, P. Kimvilakani: Appl. Opt. **36**, 5987 (1997)
3 D. Nedeljkovic, A. Hauchecorne, M.L. Chanin: IEEE Trans. Geosci. Remote Sens. **31**, 90 (1993)
4 P. Keckhut, M.L. Chanin, A. Hauchecorne: Appl. Opt. **29**, 5182 (1990)
5 J. Cooney: J. Appl. Meteorol. **11**, 108 (1972)
6 A. Cohen, J. Cooney, N. Kenneth: Appl. Opt. **15**, 2896 (1976)
7 J.A. Cooney: Appl. Opt. **23**, 653 (1984)
8 A. Behrendt, J. Reichardt: Appl. Opt. **39**, 1372 (2000)
9 Y.F. Arshinov, S.M. Bobrovnikov, V.E. Zuev, V.M. Mitev: Appl. Opt. **22**, 2984 (1983)
10 Y. Arshinov, S. Brobovnikov: Appl. Opt. **38**, 4635 (1999)
11 J.D. Klett: Appl. Opt. **20**, 211 (1981)
12 F.G. Fernald: Appl. Opt. **23**, 652 (1984)
13 A. Ansmann, M. Riebesell, C. Weitkamp: Opt. Lett. **15**, 746 (1990)
14 A. Angström: Geogr. Ann. **11**, 156 (1929)
15 G. Larcheveque, I. Balin, R. Nessler, P. Quaglia, V. Simeonov, H. van den Bergh, B. Calpini: Appl. Opt. **41**, 2781 (2002)
16 S.H. Melfi, J.D. Lawrence, M.P. McCormick: Appl. Phys. Lett. **15**, 295 (1969)
17 E.D. Hinkley: *Laser Monitoring of the Atmosphere* (Springer, Berlin 1976)
18 United States Committee on Extension to the Standard Atmosphere (COESA). US Government Printing Office, 1976
19 D.N. Whiteman, S.H. Melfi, R.A. Ferrare: Appl. Opt. **31**, 3068 (1992)
20 T. Ingold, C. Matzler, N. Kampfer, A. Heimo: J. Geophys. Res. Atmos. **106**, 27 537 (2001)
21 I. Mattis, A. Ansmann, D. Althausen, V. Jaenisch, U. Wandinger, D. Muller, Y.F. Arshinov, S.M. Bobrovnikov, I.B. Serikov: Appl. Opt. **41**, 6451 (2002)
22 B. Lazzarotto, M. Frioud, G. Larcheveque, V. Mitev, P. Quaglia, V. Simeonov, A. Thompson, H. van den Bergh, B. Calpini: Appl. Opt. **40**, 2985 (2001)
23 I. Balin, G. Larchevêque, P. Quaglia, V. Simeonov, H. van den Bergh, B. Calpini: 'Water Vapor Profile by Raman Lidar in the Free Troposphere from the Jungfraujoch Alpine Station'. In: *Climatic Changes: Implications for the Hydrological Cycle and Water Management* (Adv. Global Change Res.), ed. by M.E. Beniston (Kluwer, Dordrecht, Boston, MA 2002)
24 J. Bösenberg, M. Alpers, A. Ansmann, J.M. Baldasamo, D. Balis, C. Böckmann, B. Calpini, A. Chaikovsky, A. Hagard, V. Mitev, A. Papajanis, J. Pelon, D. Resendes, N. Spinelli, T. Trickl, G. Vaughan, G. Visconti, M. Wiegner: in *Proc. 21st Int. Laser Radar Conf. (ILRC 21)* (2002) p. 293
25 A. Ansmann, Y. Arshinov, S. Bobrovnikov, I. Mattis, I. Serikov, U. Wandinger: in *Fifth Int. Symp. Atmospheric and Ocean Optics* (1998) p. 491
26 U. Baltensperger, H.W. Gaggeler, D.T. Jost, M. Lugauer, M. Schwikowski, E. Weingartner, P. Seibert: J. Geophys. Res. Atmos. **102**, 19 707 (1997)
27 R.G. Barry: *Mountain Weather and Climate* (Routledge, London, New York 1992)